RSC Advances

PAPER

View Article Online
View Journal | View Issue

Cite this: *RSC Adv.*, 2019, **9**, 19837

A two-dimensional MoS_2/C_3N broken-gap heterostructure, a first principles study

Yaxiao Yang[ab] and Zhiguo Wang *[a]

Received 19th April 2019
Accepted 20th June 2019

DOI: 10.1039/c9ra02935d

rsc.li/rsc-advances

van der Waals (vdW) heterojunctions are of interest in two-dimensional electronic and optoelectronic devices. In this work, first-principles calculations were used to study the atomic and electronic properties of the MoS_2/C_3N vdW heterojunction. The results show that there is no overlap of the band gaps for the MoS_2 and C_3N monolayers in the heterojunction, indicating the MoS_2/C_3N vdW heterostructure has a type III alignment. The MoS_2/C_3N vdW heterostructure is a broken-gap heterojunction. The effects of biaxial strain and external electric field on the band structure of the vdW heterostructure were also investigated. The alignment type cannot be changed, but the band overlap can be tuned. The present work reveals that the MoS_2/C_3N heterostructures are quite favorable for applications in tunneling devices based on the broken-gap heterostructures.

1. Introduction

Two-dimensional (2D) materials, such as graphene, graphitic carbon nitrides and transition-metal chalcogenides (TMDs), have attracted tremendous interest because of their special physical and chemical properties[1,2] and their potential use in electronic and optoelectronic devices.[3,4] Monolayer MoS_2 is a semiconductor material with a direct band gap of 1.8 eV, which makes it a candidate for applications in photodetectors, photovoltaics, and photocatalysis.[5,6] A phototransistor was successfully made based on a MoS_2 monolayer with SiO_2 as the dielectric layer on a Si substrate.[7] A suitable band gap and high excition binding energy of the MoS_2 monolayer make it suitable for use in light emitting devices with feasible approaches to enhance their photoluminescence.[8–11] The C_3N monolayer, with a similar atomic structure to graphene, has many similar outstanding properties similar to graphene, such as high carrier mobility, quantum Hall effect, and high thermal conductivity.[12,13] C_3N is a promising candidate for applications in transistors and logic devices due to its indirect band gap, which is different from the zero band gap of graphene.[13,14]

Recently, the capability has been developed for stacking one type of 2D material on another one to form an artificial heterostructure coupled with weak van der Waals (vdW) interaction, these heterostructures are often referred as the vdW heterojunctions.[7,15] The vdW heterojunctions are of interest to 2D electronic and optoelectronic technology due to their atomically sharp interface and minimal trap states absence of dangling bonds. Vertical 2D devices based on 2D semiconductor heterojunctions have ideal band gap, high speed and larger power than traditional bulk junctions due to the short current path and large current cross.[16,17] According to the band alignment of the two dissimilar 2D materials, there exist three types of heterostructures. The heterostructures with different type interface have different applications fields. The first one is that the small bandgap material entirely lies within band gap of another one (straddling gap, type I), such band structure is useful for optoelectronic devices requiring a quantum heterostructure, such as light-emitting diodes.[18] The second one is that the band gap of one material partially overlaps with that of another one (staggered gap, type II), such band structure is beneficial for transportation carriers and dissociation of excitons, such as g-C_3N_4/CeO_2 (ref. 19) and MoS_2/SnO_2 (ref. 20) heterojunctions with type II band alignment have potential applications in photovoltaic devices.[3,21] The third one is that the bandgaps of the two materials do not overlap (broken gap, type III), such band structure is essential for the tunneling devices such as negative differential resistance (NDR) devices.[22] The diversified band alignments of vdW heterojunction are the base to building 2D vertical devices. Such as the photovoltaic detector build of a $MoTe_2/MoS_2$ heterojunction can work even under zero bias;[4] and a $Mg(OH)_2/WS_2$ heterojunction can be applied in novel nanoscale laser devices.[23]

The type-III heterojunctions based on traditional bulk materials, such as Si, Ge and III–V semiconductors have been widely studied.[24,25] However, the function of these devices maybe restricted by the dislocations result from lattice mismatch. Although nano-scale materials can be applied to solve this problem to some extent, however the increase of the bandgap will depress the performance of the devices.[25] 2D semiconductors have also attracted much attention to build

[a]Center for Public Security Technology, School of Electronic Science and Engineering, University of Electronic Science and Technology of China, Chengdu, China. E-mail: zgwang@uestc.edu.cn

[b]School of Optoelectronic Science and Engineering, University of Electronic Science and Technology of China, Chengdu, China

broken gap heterojunctions since they are free from the lattice mismatch and dangling bond, thus contributing to the superior characteristics of 2D vdW heterojunctions.[22,26] However, it requires a large electric field across the heterojunction to change type II alignment of MoS_2/WSe_2 heterostructures into type III alignment.[27] And it needs a large biaxial strain of 8% to tune the type II to type III transition in GeC/WS_2 heterostructure.[28] In this paper, we studied the atomic and electronic properties of MoS_2/C_3N vdW heterostructure by using density functional theory (DFT). It was shown that the MoS_2/C_3N vdW heterostructure with type III alignment. The effects of biaxial strain and external electric field on the band structure of the heterostructure were also investigated. The alignment type cannot be changed, but the band overlap between MoS_2 and C_3N can be tuned by the biaxial strain and electric field. These results are useful for the design of tunneling devices based on the type-III heterojunctions.

2. Computational methods

All the DFT calculations were performed by using the Vienna ab initio simulation package (VASP).[29,30] The interaction between the core and valence electrons was described using the projected augmented wave (PAW) potential.[31] Perdew–Burke–Ernzerhof (PBE) functional was used to describe the exchange and correlation interactions. An energy cutoff of 520 eV was used to expand the plane wave. The DFT-D2 method developed by Grimme[31] was used to describe the weak vdW interaction. The Brillouin zone was integrated using a Monkhorst–Pack mesh[32] of $10 \times 10 \times 1$, $6 \times 6 \times 1$ and $4 \times 4 \times 1$ *k*-points for the structural relaxation of the unit cell of MoS_2, C_3N and the MoS_2/C_3N heterostructures, respectively. And $20 \times 20 \times 1$, $16 \times 16 \times 1$ and $10 \times 10 \times 1$ *k*-points for the band structure calculation of MoS_2, C_3N and the MoS_2/C_3N heterostructures, respectively. To avoid the interaction between image atoms, the vacuum spacing of 25 Å was added on the surface of monolayers and heterostructures. All atoms and lattice parameters were by using a conjugate gradient algorithm with convergence conditions that the energy is less than 10^{-6} eV between two consecutive steps and the maximum stress on each atom is less than 0.02 eV $Å^{-1}$.

3. Results and discussion

The cross and side views of the ball-and-stick model for MoS_2 and C_3N monolayers are exhibited in Fig. 1a and b, respectively. MoS_2 monolayer is consisted of three atomic layers with the Mo layer sandwiched by S layers. The calculated lattice constant of MoS_2 monolayer is 3.192 Å. C_3N monolayer has hexagonal graphene-like structure with one N atom surrounded by three C atoms, the calculated lattice constant is 4.861 Å for C_3N monolayer. These results are in good agreement with the reports in previous work.[33,34] The MoS_2 monolayer is a semiconductor with a direct band gap of 1.65 eV with both the conduction band minimum (CBM) and the valence band maximum (VBM) locate at the K-point, which agrees with the other theoretical calculation of 1.68 eV (ref. 21) and smaller than the experimental value of 1.8 eV.[35] C_3N monolayer is an indirect band semiconductor with VBM locates at M point and the CBM located at Γ point gap. C_3N monolayer is an indirect band semiconductor with VBM locates at M point and the CBM located at Γ point gap. The band gap of C_3N monolayer is 0.39 eV which is consistent with previous report.[33] It is known that the standard DFT calculation often underestimates the band gap of materials, the band structures of MoS_2 and C_3N monolayers were further calculated with the Heyd–Scuseria–Ernzerhof hybrid functional (HSE06).[36] The band gaps of MoS_2 and C_3N monolayers calculated with HSE06 are 2.11 (direct band gap) and 1.09 eV (indirect band gap), respectively, which agrees with the previous reports.[21,35,37] A vdW heterostructure can be built by stacking the MoS_2 on C_3N. A 3×3 MoS_2 and 2×2 C_3N monolayer supercells are stacked to form the MoS_2/C_3N heterojunction in order to keep the lattice mismatch within ~1.5%. It should be noticed that the M point in the unit cell of C_3N monolayer is folded into Γ point in a 2×2 supercell, leading to the shift of VBM from M point to Γ point.[38] Thus C_3N monolayer shows a direct band gap characteristic when it is calculated with a 2×2 supercell (as shown in Fig. 1e), which has been reported in the literatures.[38–40] And the C_3N monolayer shows a direct band gap characteristic in the MoS_2/C_3N heterostructure, which is due to the folded band calculated with the supercell method caused by the shrinkage of the Brillouin zone.[39]

The most energy favorable stacking of MoS_2/C_3N heterostructure was evaluated by calculating the binding energy (E_b), $E_b = E_{hetero} - E_{MoS_2} - E_{C_3N}$, where E_{hetero}, E_{MoS_2}, and E_{C_3N} are the total energies of heterostructure, MoS_2, and C_3N monolayers, respectively. The top and side views of possible stacking patterns are shown in Fig. 2, the binding energies and the interlayer distance are listed in Table 1. The calculated binding energies (E_b) are in the range between −15.086 and −15.114 meV $Å^{-2}$, and the interlayer distance (d) between MoS_2 and C_3N monolayer in the heterostructures is in the range between 3.236 and 3.263 Å, which agrees well with reported typical values in vdW systems.[41–44] These results indicate the weak vdW interaction between the two layers. The stacking configuration in Fig. 2c with one of the Mo atom of MoS_2 monolayer coincide with a N atom of C_3N monolayer has the largest negative binding energy, which indicates that this configuration is energy favorable. The following calculations are all based on this heterostructure.

The vdW heterostructures of MoS_2 monolayer stacked on AlN (GaN) semiconductors has been well studied,[45,46] and the band alignment can be tuned by varying the thickness of GaN. The work function can be used as an intrinsic reference for the band alignment. The work functions (energy difference between fermi energy level and vacuum level) of MoS_2 monolayers are 5.66 and 5.79 eV calculated by standard DFT and HSE06 functional, respectively, which agree with the previous reports.[47,48] The work functions of C_3N monolayer are 2.93 eV and 3.39 eV calculated by standard DFT calculation and HSE06 functional, respectively. The calculated work function of C_3N monolayer is smaller than that of MoS_2 monolayers, which indicates that a broken gap vdW heterostructure may be formed for the $MoS_2/$

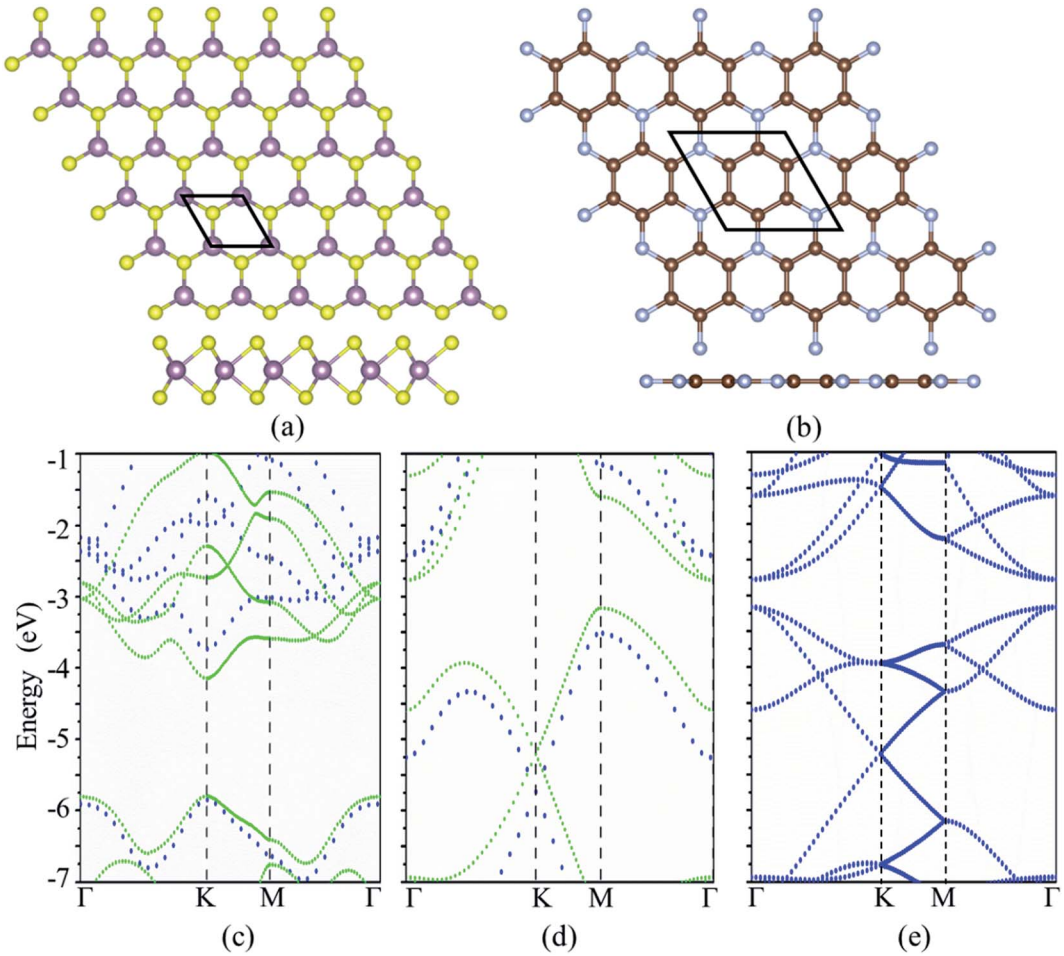

Fig. 1 The top and side view of atomic configurations for (a) MoS_2 and (b) C_3N monolayers. The purple, yellow, brown and blue balls denote Mo, S, C, and N atoms, respectively. The band structures of (c) MoS_2 and (d) C_3N monolayers, the green and blue dotted lines represent the band structures calculated with standard DFT and the HSE functional, respectively. (e) Band structure of C_3N monolayer calculated with 2 × 2 supercell.

C_3N heterostructure. The projected band structures of MoS_2/C_3N heterostructure were calculated with standard DFT and HSE functional and shown in Fig. 3a. The blue and orange dots represent the band contributions from C_3N and MoS_2 calculated with standard DFT, and the cane and green triangles represent those calculated by HSE06 functional, respectively. The corresponding band alignments calculated using standard DFT calculation and HSE functional are schematically shown in Fig. 3b and c, respectively. The MoS_2 monolayer remains its direct band gap semiconducting property, but the band gap decrease from 1.65 eV of the pristine to 1.40 eV in the heterostructure. The decease of band gap of MoS_2 monolayer has also observed in other heterostructures[21] due to the interaction between the two monolayers.

Both standard DFT and HSE06 calculations show that the VBM of C_3N is higher than the CBM of MoS_2. There is no overlap of the band gaps for MoS_2 and C_3N monolayers in the heterostructure, indicating the MoS_2/C_3N vdW heterostructure is with a type III alignment. For the standard DFT calculation, the conduction band offset (CBO) and valence band offset (VBO) are 0.63 and 2.64 eV, the band overlap ($\Delta = E^{VBM}_{C_3N} - E^{CBM}_{MoS_2}$) is 0.24 eV for the MoS_2/C_3N heterostructure. The CBO and VBO are 1.06 and 1.87 eV derived from the HSE06 calculation, and the band overlap is 0.12 eV. There exists considerable carrier migration in this sort of heterostructures even without an external electric field, it will lead to an accumulation of electrons in the MoS_2 and holes in C_3N near the junction. Under these circumstances, a highly doped p^+/n^+ heterojunction can be achieved in the MoS_2/C_3N heterostructure even without any electrostatic or chemical doping. This particular property makes it a promising material for negative differential resistance (NDR) devices.[26,49]

The electric field can be used to modulate the positions of VBM and CBM in 2D semiconductors, such as the CBM shifts to low energy as an external electric field applied perpendicular to the surface of GaGeTe monolayer.[50] The electric field also can modify the band alignment of 2D heterostructures,[26,28] such as a type II band alignment transforms to type III one as an the electric field is larger than 0.6 V $Å^{-1}$ in $MoTe_2$/WSe_2 heterostructure.[51] The effects of external electric field on the band alignment of MoS_2/C_3N heterostructure were investigated by

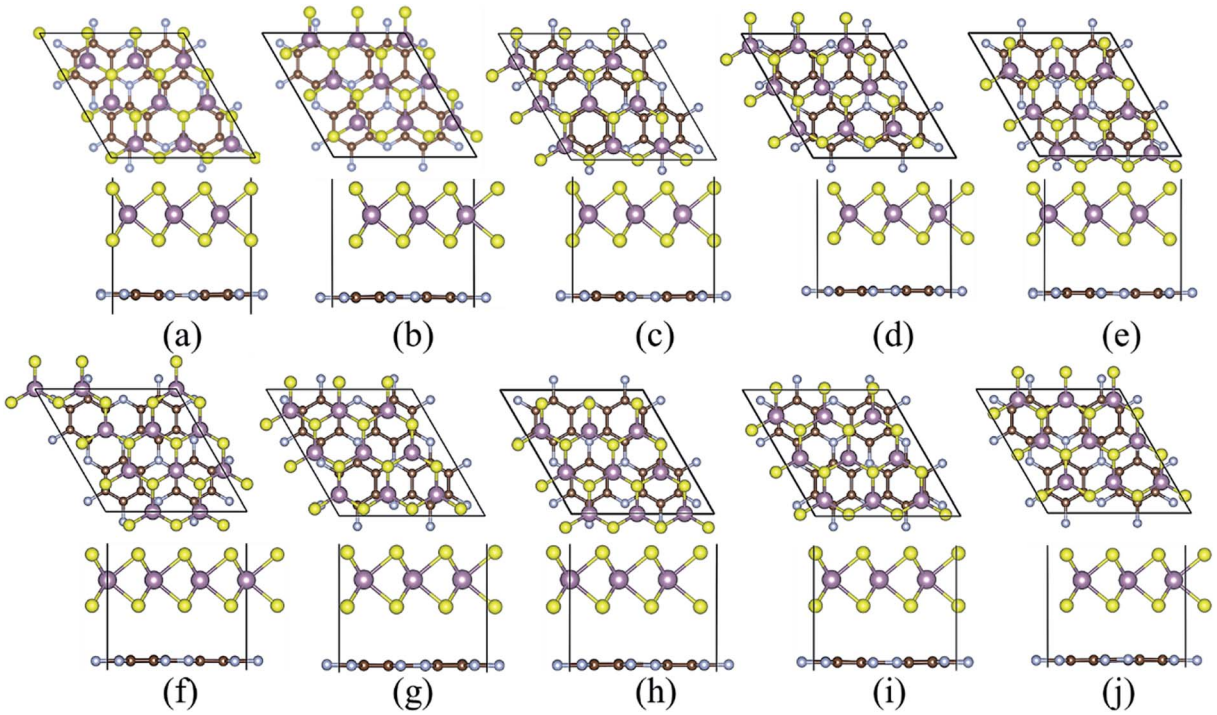

Fig. 2 The atomic structures for the 2D vdW heterojunction in different configurations of arrangement of MoS_2 monolayer on the top of C_3N. The top column is the top view, and the bottom column is the side view. The purple, yellow, brown and blue, balls denote Mo, S, C, and N atoms, respectively.

Table 1 Binding energies (E_b, meV) and distance (d, Å) between the two layers of MoS_2/C_3N heterojunction with stacking configurations shown in Fig. 2

	a	b	c	d	e	f	g	h	i	j
E_b	−15.110	−15.112	−15.114	−15.103	−15.086	−15.106	−15.103	−15.096	−15.110	−15.110
d	3.236	3.263	3.246	3.261	3.259	3.254	3.256	3.262	3.254	3.251

applying positive (along the direction from MoS_2 to C_3N) and negative (along the direction from C_3N to MoS_2) electric field. The projected band structures of MoS_2/C_3N heterostructure with external electric field are plotted in Fig. 4a. As the negative electric field is changed from 0 to -0.4 V Å^{-1}, the CBM of MoS_2 and VBM of C_3N shift upward and downward to the Fermi

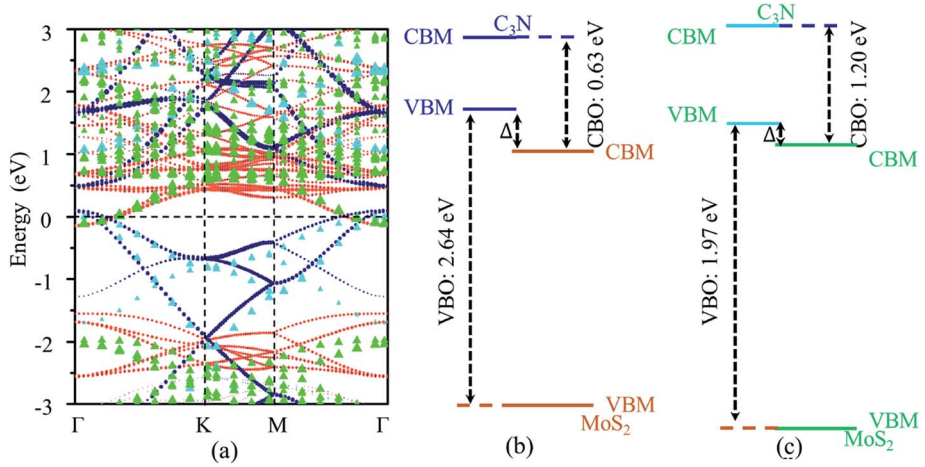

Fig. 3 (a) Projected band structure and band alignment of MoS_2/C_3N heterojunction calculated with (b) standard DFT and (c) the HSE functional. The blue dots and orange dots represent the band contributions from C_3N and MoS_2 (calculated with standard DFT), and the cane and green triangular represent those calculated by the HSE functional, respectively. The dashed line represents the Fermi energy level.

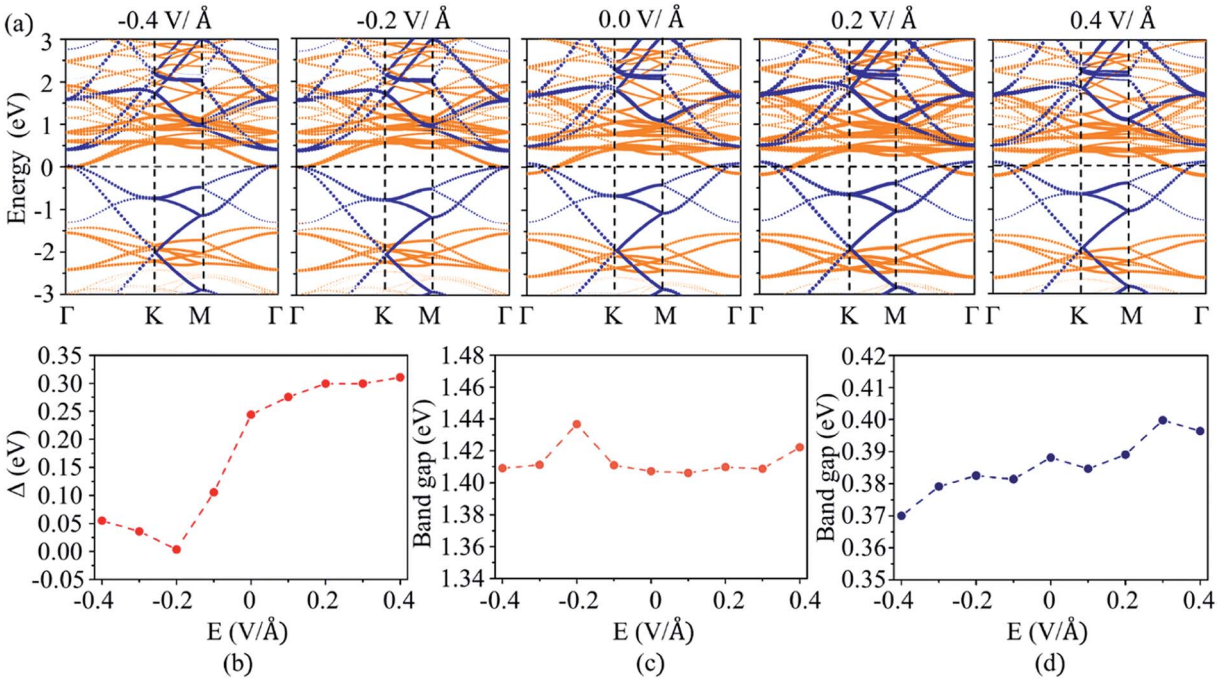

Fig. 4 (a) The projected band structures of MoS_2/C_3N heterojunction with electric field applied. The blue dots and orange dots represent the band contributions from C_3N and MoS_2, respectively. Evolution of the (b) band overlap, band gap of (c) MoS_2 and (d) C_3N as a function of the external electric field.

energy level, thus leading to the decrease in band overlap (Δ). The value of Δ is close to zero (0.004 eV) at an electric field of -0.2 V Å^{-1}. Whereas the value of Δ increases as a positive electric field applied. The evolution of Δ with the electric field is shown in Fig. 4b. Δ increases from 0.24 to 0.33 eV as the positive electric field increases from 0 to 0.4 V Å^{-1}. As can be seen from Fig. 4a, the CBM of MoS_2 monolayer remains at the Γ point, while VBM shifts from Γ point to a point between Γ and K points as negative electric field applied. Both CBM and VBM remain at the Γ point as positive electric field applied. The positive electric field does not affect the position of CBM and VBM of C_3N monolayer. The evolution of band gaps for MoS_2 and C_3N monolayers as a function of electric field is shown in Fig. 4c and d, respectively. The band gaps C_3N monolayers

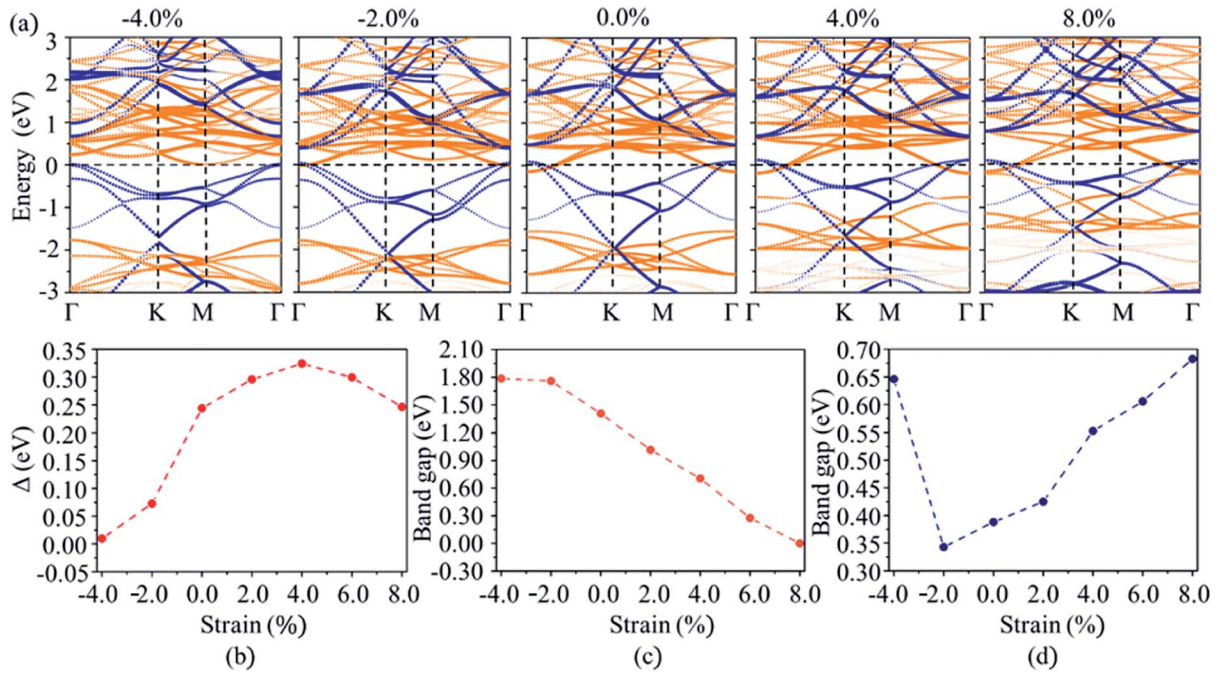

Fig. 5 (a) The projected band structures of MoS_2/C_3N heterojunction with strain applied. The blue dots and orange dots represents the band contributions from C_3N and MoS_2, respectively. Evolution of the (b) band overlap, band gap of (c) MoS_2 and (d) C_3N as a function of strain.

decreases with the increase of negative electric field and increases with the positive electric field. While band gap of MoS_2 changes a little with the electric field. These results indicate that the band structure and band alignment of MoS_2/C_3N heterostructure can be tuned by the external electric field, which can be used to tune the accumulation of holes in C_3N and electrons in MoS_2.

Except for the electric field, strain is often used to tune the electronic properties of 2D materials for meeting the requirements of application.[37,52] The modulation of strain on the electric properties of MoS_2/C_3N heterostructure was investigated by applying the in-plane biaxial strain. The strain (ε) in the range between −4% and 8% is imposed by varying the lattice parameter with $\varepsilon = \frac{a - a_0}{a_0} \times 100\%$, where a and a_0 are the lattice parameters of strain and pristine MoS_2/C_3N heterostructure. The projected band structures of MoS_2/C_3N heterostructure under strain are shown in Fig. 5a. As the tensile strain is increased from 0 to 8%, the value of Δ increases. When the strength of tensile strain is 6%, Δ reaching up to its maximum of 0.33 eV. The band overlap decreases with compressive strain as shown in Fig. 5a. As the compressive strain of −4% leads to band overlap very close to zero (0.0114 eV). Under tensile strain, the CBM of MoS_2 was not changed by the strain, but the VBM of MoS_2 moved upward with the increase in tensile strain, which leads the band gap decrease of MoS_2. The compressive strain leads the CBM of MoS_2 shifts to higher energy and VBM to lower energy, thus the band gap of MoS_2 increases with increasing compressive strain as shown in Fig. 5c. Whereas the band gap of C_3N monolayer increases with tensile strain or decreases with a compressive strain was applied, except for a large compressive strain of −4.0% (as shown in Fig. 5d). So the band alignment of MoS_2/C_3N heterostructure can also be tuned by applying a biaxial strain.

The band alignment of MoS_2/C_3N heterostructure can be tuned by external vertical electric field and strain, and MoS_2/C_3N heterostructure keep the type III band alignment under all the studied conditions, thus the MoS_2/C_3N heterostructures is quite favorable for applications in tunneling devices based on the broken-gap heterostructures.

4. Conclusion

In conclusion, the structural and electronic properties of the MoS_2/C_3N heterostructure were studied using DFT calculation. The MoS_2/C_3N heterostructure is a broken-gap heterojunction with the VBM of C_3N higher than the CBM of MoS_2. The value of Δ increases from 0.24 to 0.33 eV as a positive electric field increases from 0 to 0.4 V Å^{-1}. And the value of Δ decreases as a negative electric field is applied. The band overlap can also be tuned by bi-axil strain. Compressive strain induced the decrease of band overlap. The alignment type was not changed for both electric field and strain applied. The present work reveals that the MoS_2/C_3N heterostructures is quite favorable for applications in tunneling devices based on the broken-gap heterostructures.

Conflicts of interest

There are no conflicts of interest to declare.

References

1 S. Hussain, K. Xu, S. Ye, L. Lei, X. Liu, R. Xu, L. Xie and Z. Cheng, *Front. Phys.*, 2019, **14**, 33401.
2 K. Ren, M. Sun, Y. Luo, S. Wan, J. Yu and W. Tang, *Appl. Surf. Sci.*, 2019, **476**, 70–75.
3 W. Feng, Z. Jin, J. Yuan, J. Zhang, S. Jia, L. Dong, J. Yoon, L. Zhou, R. Vajtai, J. M. Tour, P. M. Ajayan, P. Hu and J. Lou, *2D Mater.*, 2018, **5**, 025008.
4 Y. Chen, X. Wang, G. Wu, Z. Wang, H. Fang, T. Lin, S. Sun, H. Shen, W. Hu, J. Wang, J. Sun, X. Meng and J. Chu, *Small*, 2018, **14**, 1703293.
5 A. Sengupta, A. Chanana and S. Mahapatra, *AIP Adv.*, 2015, **5**, 027101.
6 M. Sun, P. Yang, D. Xie, Y. Sun, J. Xu, T. Ren and Y. Zhang, *Adv. Electrode Mater.*, 2019, **5**, 1800580.
7 H. Li, J. Wu, Z. Yin and H. Zhang, *Acc. Chem. Res.*, 2014, **47**, 1067–1075.
8 W. Su, H. Dou, J. Li, D. Huo, N. Dai and L. Yang, *RSC Adv.*, 2015, **5**, 82924–82929.
9 M. Buscema, G. A. Steele, H. S. J. van der Zant and A. Castellanos-Gomez, *Nano Res.*, 2014, **7**, 561–571.
10 W. Su, H. Dou, D. Huo, N. Dai and L. Yang, *Chem. Phys. Lett.*, 2015, **635**, 40–44.
11 S. Mouri, Y. Miyauchi and K. Matsuda, *Nano Lett.*, 2013, **13**, 5944–5948.
12 B. Mortazavi, *Carbon*, 2017, **118**, 25–34.
13 X. Zhou, W. Feng, S. Guan, B. Fu, W. Su and Y. Yao, *J. Mater. Res.*, 2017, **32**, 2993–3001.
14 M. Makaremi, B. Mortazavi and C. V. Singh, *J. Phys. Chem. C*, 2017, **121**, 18575–18583.
15 Y. Deng, Z. Luo, N. J. Conrad, H. Liu, Y. Gong, S. Najmaei, P. M. Ajayan, J. Lou, X. Xu and P. D. Ye, *ACS Nano*, 2014, **8**, 8292–8299.
16 J. Yan, Y. Hao, Y. Cui, J. Zhang, Y. Zou, W. Zhang, G. Yu, J. Zheng, W. Xu and D. Zhu, *J. Mater. Chem. C*, 2018, **6**, 12976–12980.
17 K. H. Chan, S. M. Ng, H. F. Wong, C. W. Leung and C. L. Mak, *Phys. Status Solidi A*, 2019, **216**, 1800829.
18 K. Tang, W. Qi, Y. Li and T. Wang, *Phys. Chem. Chem. Phys.*, 2018, **20**, 29333–29340.
19 Q. Qiao, K. Yang, L. L. Ma, W. Q. Huang, B. X. Zhou, A. Pan, W. Hu, X. Fan and G. F. Huang, *J. Phys. D*, 2018, **51**, 275302.
20 S. S. Ding, W. Q. Huang, Y. C. Yang, B. X. Zhou, W. Y. Hu, M. Q. Long, P. Peng and G. F. Huang, *J. Appl. Phys.*, 2016, **119**, 205704.
21 C. Liao, Y. Zhao and G. Ouyang, *ACS Omega*, 2018, **3**, 14641–14649.
22 J. Shim, S. Oh, D. H. Kang, S. H. Jo, M. H. Ali, W. Y. Choi, K. Heo, J. Jeon, S. Lee, M. Kim, Y. J. Song and J. H. Park, *Nat. Commun.*, 2016, **7**, 13413.
23 M. Yagmurcukardes, E. Torun, R. T. Senger, F. M. Peeters and H. Sahin, *Phys. Rev. B*, 2016, **94**, 195403.

24 C. Grillet, A. Cresti and M. G. Pala, *IEEE Trans. Electron Devices*, 2018, **65**, 3038–3044.
25 S. Alagha, S. Zhao, Z. Mi, S. P. Watkins and K. L. Kavanagh, *IEEE Trans. Electron Devices*, 2018, **33**, 015008.
26 R. Yan, S. Fathipour, Y. Han, B. Song, S. Xiao, M. Li, N. Ma, V. Protasenko, D. A. Muller, D. Jena and H. G. Xing, *Nano Lett.*, 2015, **15**, 5791–5798.
27 J. Shim, D. H. Kang, Y. Kim, H. Kum, W. Kong, S. H. Bae, I. Almansouri, K. Lee, J. H. Park and J. Kim, *Carbon*, 2018, **133**, 78–89.
28 J. Shi, Y. Ou, M. A. Mighorato, H. Wang, H. Li, Y. Zhang, Y. Gu and M. Zou, *Comput. Mater. Sci.*, 2019, **160**, 301–308.
29 P. J. Stephens, F. J. Devlin, C. F. Chabalowski and M. J. Frisch, *J. Phys. Chem.*, 1994, **98**, 11623–11627.
30 M. Brandbyge, J. L. Mozos, P. Ordejon, J. Taylor and K. Stokbro, *Phys. Rev. B: Condens. Matter Mater. Phys.*, 2002, **65**, 165401.
31 G. Kresse and D. Joubert, *Phys. Rev. B: Condens. Matter Mater. Phys.*, 1999, **59**, 1758–1775.
32 H. J. Monkhorst and J. D. Pack, *Phys. Rev. B: Solid State*, 1976, **13**, 5188–5192.
33 M. B. Tagani, *Comput. Mater. Sci.*, 2018, **153**, 126–133.
34 A. Slassi and J. Cornil, *2D Mater.*, 2018, **6**, 015025.
35 K. F. Mak, C. Lee, J. Hone, J. Shan and T. F. Heinz, *Phys. Rev. Lett.*, 2010, **105**, 136805.
36 J. Heyd, G. E. Scuseria and M. Ernzerhof, *J. Chem. Phys.*, 2003, **118**, 8207–8215.
37 L. B. Shi, M. B. Li, X. M. Xiu, X. Y. Liu, K. C. Zhang, Y. H. Liu, C. R. Li and H. K. Dong, *J. Appl. Phys.*, 2017, **121**, 205305.
38 X. Wang, Q. Li, H. Wang, Y. Gao, J. Hou and J. Shao, *Phys. B*, 2018, **537**, 314–319.
39 L. Xie, L. Yang, W. Ge, X. Wang and J. Jiang, *Chem. Phys.*, 2019, **520**, 40–46.
40 X. Gao, Y. Shen, Y. Ma, S. Wu and Z. Zhou, *Appl. Surf. Sci.*, 2019, **479**, 1098–1104.
41 T. Bjorkman, A. Gulans, A. V. Krasheninnikov and R. M. Nieminen, *Phys. Rev. Lett.*, 2012, **108**, 235502.
42 T. Bjorkman, A. Gulans, A. V. Krasheninnikov and R. M. Nieminen, *J. Phys.: Condens. Matter*, 2012, **24**, 424218.
43 Y. C. Yang, L. Xu, W. Q. Huang, C. Y. Luo, G. F. Huang and P. Peng, *J. Phys. Chem. C*, 2015, **119**, 19095–19104.
44 C. F. Fu, R. Zhang, Q. Luo, X. Li and J. Yang, *J. Comput. Chem.*, 2019, **40**, 980–987.
45 J. Liao, B. Sa, J. Zhou, R. Ahuja and Z. Sun, *J. Phys. Chem. C*, 2014, **118**, 17594–17599.
46 J. Wang, H. Shu, P. Liang, N. Wang, D. Cao and X. Chen, *J. Phys. Chem. C*, 2019, **123**, 3861–3867.
47 P. Wu, M. Huang, N. Yin and P. Li, *Nanomaterials*, 2019, **9**, 395.
48 S. Kwon, S. H. Choi, Y. J. Kim, I. T. Yoon and W. Yang, *Thin Solid Films*, 2018, **660**, 766–770.
49 H. Kroemer, *Phys. Scr.*, 1996, **T68**, 10–16.
50 C. Ke, Y. Wu, J. Zhou, Z. Wu, C. Zhang, X. Li and J. Kang, *J. Phys. D*, 2019, **52**, 115101.
51 Y. Liu and X. Cheng, *Phys. E*, 2019, **108**, 90–95.
52 H. Aramberri and M. C. Munoz, *Phys. Rev. B*, 2017, **95**, 205422.